CDDpress

www.nature.com/cdd

ARTICLE

Ferroptosis mediates selective motor neuron death in amyotrophic lateral sclerosis

Taide Wang[1], Doris Tomas[1], Nirma D. Perera[1], Brittany Cuic[1], Sophia Luikinga[1], Aida Viden[1], Samantha K. Barton[1], Catriona A. McLean[2], André L. Samson[3,4], Adam Southon[1], Ashley I. Bush[1], James M. Murphy[3,4] and Bradley J. Turner[1,5]✉

Amyotrophic lateral sclerosis (ALS) is caused by selective degeneration of motor neurons in the brain and spinal cord; however, the primary cell death pathway(s) mediating motor neuron demise remain elusive. We recently established that necroptosis, an inflammatory form of regulated cell death, was dispensable for motor neuron death in a mouse model of ALS, implicating other forms of cell death. Here, we confirm these findings in ALS patients, showing a lack of expression of key necroptotic effector proteins in spinal cords. Rather, we uncover evidence for ferroptosis, a recently discovered iron-dependent form of regulated cell death, in ALS. Depletion of glutathione peroxidase 4 (GPX4), an anti-oxidant enzyme and central repressor of ferroptosis, occurred in post-mortem spinal cords of both sporadic and familial ALS patients. GPX4 depletion was also an early and universal feature of spinal cords and brains of transgenic mutant superoxide dismutase 1 ($SOD1^{G93A}$), TDP-43 and C9orf72 mouse models of ALS. GPX4 depletion and ferroptosis were linked to impaired NRF2 signalling and dysregulation of glutathione synthesis and iron-binding proteins. Novel BAC transgenic mice overexpressing human GPX4 exhibited high GPX4 expression localised to spinal motor neurons. Human GPX4 overexpression in $SOD1^{G93A}$ mice significantly delayed disease onset, improved locomotor function and prolonged lifespan, which was attributed to attenuated lipid peroxidation and motor neuron preservation. Our study discovers a new role for ferroptosis in mediating motor neuron death in ALS, supporting the use of anti-ferroptotic therapeutic strategies, such as GPX4 pathway induction and upregulation, for ALS treatment.

Cell Death & Differentiation (2022) 29:1187–1198; https://doi.org/10.1038/s41418-021-00910-z

INTRODUCTION

Amyotrophic lateral sclerosis (ALS) is a rapidly progressive and universally fatal disease resulting from the selective death of motor neurons in the brain and spinal cord. Motor neuron loss results in muscle atrophy, weakness and paralysis, leading to death typically within 3–5 years from ALS onset [1]. Mutations in superoxide dismutase 1 (SOD1), TAR DNA binding protein 43 (TDP-43) and chromosome 9 open reading frame 72 (C9orf72) are common genetic causes of ALS and mouse models expressing human mutant SOD1, TDP-43 and C9orf72 develop progressive symptoms and motor neuron loss consistent with ALS [2]. Motor neuron death is recognised to be both cell and non-cell autonomous in ALS, the latter mediated in part by surrounding toxic astrocytes, microglia and oligodendrocytes [2].

Despite over 170 years since Charcot's seminal discovery of the neuropathological hallmark of ALS, selective motor neuron degeneration, the primary cell death mechanism(s) responsible for motor neuron death, remains equivocal, which has significantly hampered effective therapy development. Cell death is broadly classified as accidental or regulated cell death (RCD) [3], where RCD is further divided into apoptotic or non-apoptotic programmes of cell death. Motor neuron death was originally proposed to be apoptotic, triggered by activation of death receptors, such as Fas ligand, tumour necrosis factor or p75 neurotrophin receptors, or by triggering of the intrinsic mitochondrial pathway leading to caspase activation [4]. However, it has since been shown that pharmacological and genetic inhibition of apoptosis does not confer motor neuron protection in ALS models [5]. Furthermore, genetic ablation of endoplasmic reticulum (ER) stress-induced apoptosis was not effective in mutant SOD1 mice [6]. These findings stimulated interest in non-apoptotic modes of motor neuron death, leading to the implication of necroptosis in ALS. Necroptosis, an inflammatory form of RCD, is regarded as caspase-independent, but not always, and is typically induced by pro-inflammatory cytokines and death ligands released by inflammatory cells, such as astrocytes and microglia, leading to activation of receptor interacting kinase 1 (RIPK1), RIPK3 and mixed lineage kinase domain-like protein (MLKL) [7]. Motor neuron death was reported to be necroptosis-dependent in vitro [5]; however, evidence for a role of necroptosis in vivo in ALS is controversial [8]. Firstly, treatment with the RIPK1 inhibitor, Necrostatin-1s (Nec-1s), was reported to be beneficial [9], while in contrast knockin of a kinase-dead RIPK1 allele had no impact in $SOD1^{G93A}$ mice [10], suggesting potential off-target effects of Nec-1s. Next, genetic deletion of RIPK3 in $SOD1^{G93A}$ mice was protective in

[1]Florey Institute of Neuroscience and Mental Health, University of Melbourne, Parkville, VIC 3052, Australia. [2]Department of Anatomical Pathology, Alfred Health, Melbourne, VIC 3004, Australia. [3]The Walter and Eliza Hall Institute of Medical Research, Parkville, VIC 3052, Australia. [4]Department of Medical Biology, University of Melbourne, Parkville, VIC 3050, Australia. [5]Perron Institute for Neurological and Translational Science, Queen Elizabeth Medical Centre, Nedlands, WA, Australia. ✉email: bradley.turner@florey.edu.au
Edited by G. Melino

Received: 18 August 2021 Revised: 17 November 2021 Accepted: 18 November 2021
Published online: 2 December 2021

one study [9], but not another [11]. Finally, RIPK1, RIPK3 and MLKL were detected in spinal cords of ALS patients and SOD1^{G93A} mice in one study [9], but not others [10, 11]. To address this important disparity, we eliminated the critical effector of necroptotic cell death, MLKL, in SOD1^{G93A} mice, revealing no impact on disease onset, progression or motor neuron loss [12]. Furthermore, we could not detect RIPK3 or MLKL in whole tissue extracts by western blotting or at the level of single motor neurons using RNAScope in CNS tissues of healthy or SOD1^{G93A} mice, arguing against a role for necroptosis in ALS and, more broadly, neurodegenerative diseases.

We therefore sought to investigate alternative cell death mechanism(s) operating in ALS. Ferroptosis is a recently described RCD pathway that is increasing implicated in neurodegenerative diseases. Ferroptosis is an iron-dependent and caspase-independent form of cell death caused by toxic lipid peroxidation, leading to plasma membrane disruption and necrotic-like cell death [13–15]. Ferroptosis is regulated by a complex system of integrated oxidant and anti-oxidant pathways. The oxidant pathway is mediated by intracellular iron uptake, accumulation and redox metabolism, leading to formation of lethal lipid peroxides that damage cell membranes [14]. Iron-binding proteins such as transferrin receptor 1 (TFR1) and ferritin are key mediators of intracellular iron loading driving ferroptosis [16, 17]. However, ferroptosis is mainly triggered by inactivation of the glutathione (GSH)-glutathione peroxidase 4 (GPX4) anti-oxidant defence checkpoint, leading to accumulation of toxic lipid peroxides [14]. GPX4 is a selenocysteine-containing enzyme that counters lipid peroxide formation by oxidising its substrate, glutathione. Prior to the naming of ferroptosis, it was established that depletion of GPX4 caused degeneration of cortical and hippocampal neurons, and interneurons in mice [18, 19]. GPX4 is therefore considered the master negative regulator of ferroptosis in cells and is critical for inhibition of ferroptosis [20, 21].

It is well established from separate studies that the canonical features of ferroptosis, iron dysregulation, abnormal GSH metabolism and lipid peroxidation occur in ALS. Iron accumulation was reported decades ago in motor cortex and spinal cord of ALS patients [22, 23] and SOD1^{G93A} mice [24], and was linked to aberrant redox chemistry and oxidative stress. Next, GSH depletion was a feature of affected CNS tissues of ALS patients [25, 26] and SOD1^{G93A} mice [27], and was linked to dysregulation of the GSH uptake regulator, system x_c^-, in mutant SOD1 mice [28]. Lastly, ALS patients and mutant SOD1 mice are characterised by prominent lipid peroxidation in affected CNS tissues [29, 30]. Furthermore, neuron-specific deletion of *Gpx4* in mice resulted in muscle atrophy, paralysis and motor neuron degeneration, implicating GPX4 expression in cell vulnerability in ALS [31]. Based on these disparate lines of evidence and integrating these observations, we proposed that ferroptosis contributes to motor neuron death in ALS. Here, we investigated the central repressor of ferroptosis, GPX4, in ALS patients and multiple mouse models of ALS. We demonstrate that GPX4 depletion, which heralds ferroptosis initiation, occurs widely in spinal cords and motor neurons of ALS patients and mouse models. We further validated these findings by generating novel human GPX4 transgenic mice, which revealed that GPX4 overexpression in SOD1^{G93A} mice significantly mitigates symptoms and motor neuron loss. These findings are also consistent with a recent study that crossed SOD1^{G93A} mice with independent GPX4 transgenic mice [32]. Our results demonstrate a key role for ferroptosis in mediating motor neuron death in ALS.

MATERIALS AND METHODS

Transgenic mice

All animal experiments were performed in accordance with the Australian National Health and Medical Research Council published Code of Practice and were approved by the Florey Institute Animal Ethics Committee (permit numbers: 17-093 and 19-067). All mice in the study were kept under specific pathogen-free conditions. Animals were group-housed in microisolator cages with access to water and food ad libitum, under a standard 12 h light–dark cycle. Transgenic SOD1^{G93A} (B6.Cg-Tg(SOD1^{G93A})1Gur/J line, stock number 002726), TDP-43^{Q331K} (B6N.Cg-Tg(Prnp-TARDBP*Q331K)103Dwc/J, stock number 017933) and C9orf72^{500} (FVB/NJ-Tg(C9orf72)500Lpwr/J, stock number 029099) mice were purchased from the Jackson Laboratory (Bar Harbor, ME, USA) and maintained on C57BL/6J, C57BL/6NJ and FVB/NJ backgrounds, respectively. Strain-matched non-transgenic littermates were used as wild-type (WT) controls for each model. Mice were randomly assigned to groups with equal litter contribution. Group sizes were based on the recommended preclinical study guidelines of the ALS Therapy Development Institute [33].

Construction of transgenic GPX4 mice

Four lines of bacterial artificial chromosome (BAC) transgenic human GPX4 mice (lines 1–4) were generated using the PiggyBac™ transposon system by Cyagen Biosciences (Guangzhou, China). Briefly, a 185 kb BAC vector (clone RP11-878J15) containing the entire human *GPX4* locus was obtained. A 3′-inverted terminal repeat (ITR) sequence with an ampicillin selection cassette was introduced 20 kb downstream of *GPX4*. A 5′-ITR with a kanamycin selection cassette was introduced 10 kb upstream of GPX4. The GPX4 BAC transgene was excised by a PiggyBac transposase (PBase) and microinjected into fertilised C57BL/6N mouse eggs and implanted into surrogate mothers. Positive founders were identified using PCR genotyping of tail DNA using human GPX4 primers 5′-AAGGACCTGCCCCAC-TATTTCTA-3′ (forward) and 5′-TGTCTGTTTATTCCCACAAGGTAG-3′ (reverse) and exclusion of the PBase plasmid using primers 5′-CTGGACGAGCA-GAACGTGATCG-3′ (forward) and 5′-CGAAGAAGGCGTAGATCTCGTCCTC-3′ (reverse). Heterozygote transgenic GPX4 mice were maintained on a C57BL/6N background. Non-transgenic C57BL/6N littermates were used as WT controls. Male transgenic SOD1^{G93A} mice were crossed with female GPX4 mice to generate four isogenic genotypes for study: SOD1^{G93A};GPX4, SOD1^{G93A}, GPX4 and WT. Mice were genotyped by Transnetyx (Cordova, TN, USA). SOD1^{G93A} transgene copy numbers of all experimental mice were checked using qPCR analysis of gDNA extracted from tail biopsies and confirmed as equivalent.

Human tissues

This study was approved by the University of Melbourne Biomedical Sciences Human Ethics Advisory Group and the Medicine and Dentistry Human Ethics Sub-Committee (Project 18.36, ethics number 1852824). Lumbar spinal cord tissue was obtained from subjects with written informed consent by the Victorian Brain Bank and micro-dissected by Dr Samantha Barton. Five sporadic, five familial and one SOD1 ALS cases were obtained. All patients selected showed spinal-onset of disease (upper and/or lower limb) to reduce clinical heterogeneity. The clinical diagnosis of ALS was confirmed at post-mortem. Control lumbar spinal cords were obtained from five individuals without evidence for neurological or psychiatric disease. Tissues were fresh-frozen in liquid nitrogen and stored at −80 °C.

Behavioural and survival analysis

Mice were assessed weekly from postnatal day 60 (P60) for body weight change and locomotor function ($n = 12$ per group). Motor co-ordination was assessed weekly using a rotarod (Mouse Rotarod, 47600, Ugo Basile). Training and testing sessions for the Rotarod were as previously described [12]. SOD1^{G93A} and SOD1^{G93A};GPX4 mice were killed at clinical endpoint defined by either onset of paralysis of hindlimbs, or 20% weight loss from peak body weight. WT and GPX4 mice were culled when the last SOD1^{G93A} mouse was culled. Mice were killed by lethal injection (sodium pentobarbitone, 100 mg/kg, IP injection) at clinical endpoint or stated time points.

Histology

Mice ($n = 5$ per group) were transcardially perfused with phosphate buffered saline (PBS) followed by 4% (w/v) paraformaldehyde in phosphate buffer (0.1 M), pH 7.4. Lumbar spinal cords (L1–3) were dissected and post-fixed in formalin 10% (w/v). Paraformaldehyde-fixed and paraffin-embedded lumbar spinal cord (L1–3) (5 µm thick) mounted onto glass slides were deparaffinized and hydrated in a downgraded alcohol series. The rest of the lumbar spinal cord (L4–5) was dissected and post-fixed in 4% (w/v) paraformaldehyde in room temperature (RT) for 2 h. Lumbar spinal cords (L4–5) were then stored in sucrose (30% (w/v)) in PBS at 4 °C

until sunken. Spinal cords then were embedded in optimal cutting temperature medium and were frozen on foil over dry ice and stored at −80 °C. Cross-sections of 20 µm were cut by the cryostat following being mounted onto SuperFrost® Ultra Plus slides.

Motor neuron count

Cryosections were stained with 0.5% (w/v) cresyl violet using a standard protocol as previously described [12]. Briefly, Nissl-positive motor neurons were identified by neuronal morphology with >20 µm size and distinctive nucleolar profile. Motor neurons were counted from a total of 12 ventral horns per mouse at equally spaced intervals ($n = 5$ mice per group). Representative images were taken on a Zeiss Primo Star bright field microscope using a ×40 magnification.

Immunohistochemistry

Antigen retrieval was first conducted on paraffin sections, and slides were incubated at 95 °C in citrate buffer (0.21% (w/v) citrate, pH 6.0) for 10 min. Slides were then washed with Milli-Q water followed by two washes of PBS on a shaker with 5-min intervals. Slides were then blocked at RT in 0.5% (v/v) Triton X-100 and 10% (v/v) donkey serum in PBS for 1 h. Blocking buffer was then removed and primary antibodies including rabbit anti-GPX4 (1:100, Abcam, ab125066) and mouse anti-NeuN (1:100, Millipore, MAB377) were added in 0.1% (v/v) Triton X-100 and 1% (v/v) donkey serum in PBS at RT overnight. The next day, sections were washed three times in PBS at 5-min intervals and blocked with the same blocking solution. Blocking solution was discarded and slides were incubated with secondary antibodies for 2 h at RT with the antibody diluent. Secondary antibodies included anti-rabbit Alexa Flour 488 (1:400, Jackson ImmunoResearch, 711-545-152) and anti-mouse Alexa Fluor 647 (1:200, Thermo Fisher, A-31571). Microscopy was performed on a Zeiss LMS 780 confocal laser scanning microscope (Carl Zeiss AG, Oberkochen, Germany) using a 20x/0.8 air objective to capture the ventral horn and a 63x/1.4 oil immersion objective at resolution determined by Nyquist sampling theorem to capture the level of expression in individual motor neurons.

Protein extraction and quantification

Mice ($n = 5$ per group) were transcardially perfused with PBS to first eliminate blood. Forebrain, spinal cord (lumbar), brainstem, spleen, kidney, lung, heart, gastrocnemius, and tibialis anterior muscle were dissected and snap-frozen at (−80 °C). Both human post-mortem spinal cord and mouse tissues were thawed and homogenised in ice-cold RIPA buffer (1% (v/v) TX-100, 50 mM Tris-Cl (pH 7.4), 150 mM NaCl, 0.1% (w/v) SDS (Amresco, 0227), 1% (w/v) sodium deoxycholate (Sigma, D6750) with freshly added phosphatase inhibitors (50 mM NaF and 10 mM Na_3VO_4) and 1% (v/v) mammalian protease inhibitor cocktail (Sigma). Sonication was conducted at 50% output (Q55 Sonicator, Sonica, Newtown, CT, USA) with brief pulses applied over 5–10 s until tissue particulates were no longer visible. Samples were then stored on ice for 20 min and centrifuged at 21,000 *g* for 20 min at 4 °C to collect supernatants. Concentration of supernatants were quantified by using the BCA standard kit from Thermo Fisher (Pierce® BCA assay kit, Thermo Fisher, 23225). Samples (30 µg for all extracts) were denatured by boiling in Laemmli 5× buffer containing 10% (v/v) β-mercaptoethanol.

Immunoblotting

Protein were samples loaded into 4–20% Mini-PROTEAN® TGX Stain-Free™ gels or 4–15% Criterion™ TGX Stain-Free™ gels (Bio-Rad) in running buffer (14.8% (w/v) glycine, 0.1% (w/v) SDS, in 100 mM Tris-HCl (pH 8.2) and were separated by electrophoresis. Proteins on gel were then transferred onto 0.45 µm LF (low fluorescence) PVDF membrane (Bio-Rad) with the Trans-Blot® Turbo™ Transfer System (Bio-Rad) at 25 V for 10 min. For xCT blot, protein transfer was conducted using wet-transfer cassette overnight at 30 V at 4 °C. Membranes were followed by blocking for 1 h at RT with 5% (w/v) low fat milk powder in TBS with the addition of 0.5% (v/v) Tween-20, pH 8.0 (TBST). Membranes were then washed three times with TBST at 10-min intervals. Primary antibodies were then diluted in 3% (w/v) BSA in TBST and added for incubation for overnight at 4 °C. Primary antibodies included rabbit (Rb) anti-GPX4 (1:1,000, Abcam, ab125066), Rb anti RIPK1 (1:1000, Cell Signaling Technology, #892), rat anti-MLKL (1:1000, Millipore, MABC604), Rb anti-FTH1 (1:1000, Abcam, ab75973), Rb anti-TFR1 (1:250, Thermo Fisher, H68.4), Rb anti-GCLC (1:1000, Abcam, ab53179), Rb anti-xCT (1:1000, Abcam, ab37185), Rb anti-NRF2 (1:1000, Abcam, ab31163) and mouse anti-βIII tubulin (1:1000, Promega, G7121). The following day, membranes were washed with TBST three times with 10-min intervals. Secondary antibodies including rhodamine anti-β-actin (1:5,000, Bio-Rad, 12004163), either IRDYE 680 or 800CW, or both, were added to the blot at RT in TBST for 1 h. Following incubation, blots were washed three times at 10-min intervals. All membrane images were taken on the ChemiDoc™ MP (Bio-Rad). For analysis, blots were quantified using the ImageJ software (Rasband WS, NIH, Bethesda, MD, http://rsb.info.nih). After subtracting background intensity, values of the mean grey bands for the target protein were normalised to respective the β-actin value (or βIII where appropriate). All results were expressed as a percentage of WT for mice, and non-neurological controls for human tissues (100%).

Cell culture

HT-29 cells were maintained in Dulbecco's Modified Eagle Medium (Life Technologies) containing 8% (v/v) heat-inactivated foetal calf serum, 2 mM L-Glutamine/-GlutaMAX (Thermo Fisher Scientific, #35050061), 50 U/ml penicillin and 50 U/ml streptomycin. $MLKL^{-/-}$ HT-29 cells have been previously reported [34].

Malondialdehyde assay

Malondialdehyde (MDA) levels were quantified with a thiobarbituric acid-based assay according to the manufacturer's protocol (Lipid Peroxidation (MDA) Assay kit, Abcam, ab118970). Brain tissue ($n = 5$ mice per group) was resuspended in the supplied lysis buffer with butylated hydroxytoluene to prevent lipid peroxidation during processing. Samples were homogenised on ice for 30 s with a micropestle (Micro Tube Homogenizer System, Thomas Scientific) and then sonicated. Supernatants were collected and quantified for total protein as described above. Fluorescence (excitation 532 nm, emission 553 nm) was measured with a Clariostar plate reader (BMG Labtech). MDA levels were expressed relative to protein levels.

RNA extraction and qRT-PCR

RNA was extracted from spinal cords ($n = 5$ mice per group) with the RNeasy Mini kit (Qiagen) as per the manufacturer's instructions. RNA quality was determined using the NanoDrop One/One^c (Thermo Fisher). cDNA was then synthesised from 50 ng of total RNA with the PrimeScriptT RT kit (Takara). Primers including Gpx4 [35] were synthesised by Sigma for qPCR.

Gpx4 forward: 5′-CGCAGCCGTTCTTATCAATG-3′
Gpx4 reverse: 5′-CACTGTGGAAATGGATGAAAGTC-3′
mGpx4 forward: 5′CACTGTGGAAATGGATGAAAGTC-3
mGpx4 reverse: 5′-CTTACTTAAGCCAGCACTGC-3′
Gapdh forward: TGTGATGGGTGTGAACCACGAGAA-3′
Gapdh reverse: 5′-GAGCCCTTCCACAATGCCAAAGTT-3′

Real-time qPCR was carried out using SYBR® Premix Ex TaqTM II (Takara) with a total volume of 20 µl; 10 µl SYBR® Premix Ex TaqTM II, 10 µM of each primer and 1 µl of cDNA from five samples per group in triplicate. Relative gene expression normalised to mouse *Gapdh* was determined using the ΔCt method [36].

Statistical analyses

The investigators were blinded to genotypes for animal behaviour, histology and MDA assay. No animals or samples were excluded from analysis. All analyses were conducted using GraphPad Prism 9.0 software (San Diego, CA, USA, RRID:SCR_002798). Data points were presented as mean ± SEM. Normal distribution of data was determined using the Kolmogorov–Smirnov test. Variance between groups was similar as assessed by Bartlett's test for one-way ANOVA. Motor neuron counts, age of peak body weight, disease onset, western blot and MDA assay data were analysed using the Student's two-sided unpaired *t*-test or one-way ANOVA with Tukey's post hoc test where appropriate unless stated otherwise. Weight gain and motor function were analysed by two-way ANOVA with Tukey's post hoc test. Survival curves were analysed using the Log-rank (Mantel-Cox) test with the median values reported.

RESULTS

GPX4 is downregulated in familial and sporadic ALS patient spinal cords

We recently demonstrated a lack of necroptotic pathway effectors in CNS tissues of healthy and transgenic $SOD1^{G93A}$ mice [12]. To determine whether these findings in mice were representative of human tissue, expression of the necroptotic mediators RIPK1 and MLKL were examined in spinal cord samples of non-neurological

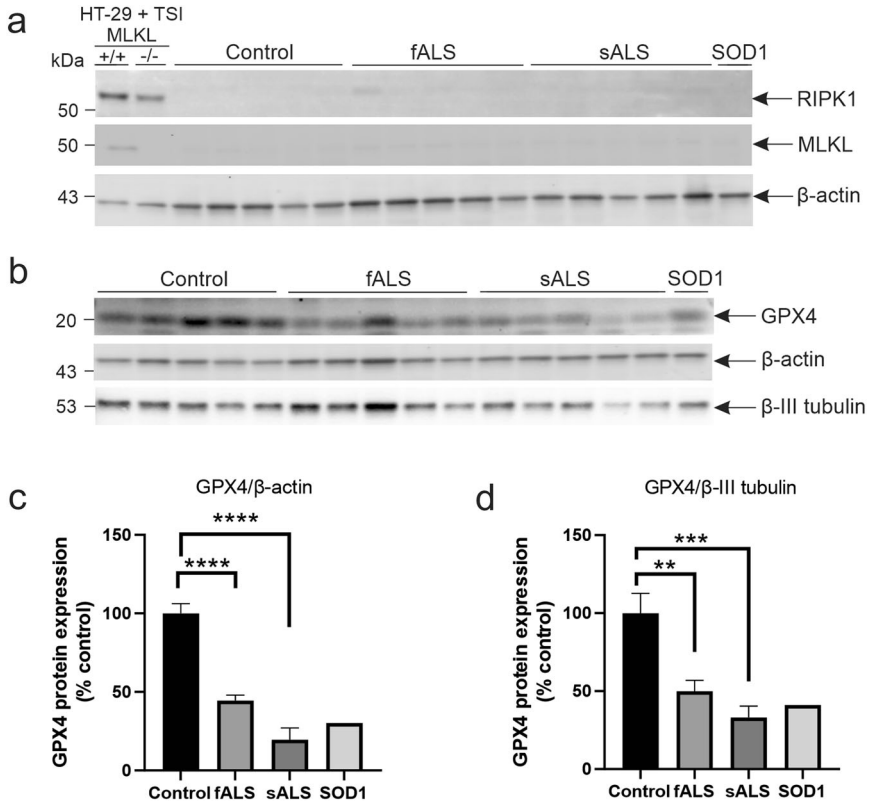

Fig. 1 Necroptotic and ferroptotic mediator expression in the spinal cords of familial and sporadic ALS patients. a Immunoblot of necroptotic markers, RIPK1 and MLKL, in spinal cords of non-neurological, familial (fALS) and sporadic ALS (sALS) patients. Specificity of the MLKL antibody was confirmed using lysates from wild-type of *MLKL*$^{-/-}$ HT-29 cells treated with necroptotic stimuli (TSI). **b** Immunoblot and quantification of GPX4 in spinal cords of fALS and sALS patients, compared to non-neurological controls, relative to **c** β-actin and **d** β-III tubulin levels. $^{**}p < 0.01$, $^{***}p < 0.001$, $^{****}p < 0.0001$; one-way ANOVA with Tukey's post hoc test. Data represent mean ± SEM, $n = 5$ cases per group, except for fALS-SOD1 ($n = 1$).

controls, familial (fALS) and sporadic ALS (sALS) patients. Lysates of WT and MLKL-deficient HT-29 cell lines treated with necroptotic stimuli [37] were used as positive and negative controls. RIPK1 and MLKL were detected in WT HT-29 cells at ~75 and ~55 kDa, respectively, while MLKL was not detected in MLKL-deficient cells (Fig. 1a). In contrast to a previous study in human post-mortem spinal cords [9], neither MLKL nor RIPK1 were detected in spinal cords from either ALS patients or non-neurological controls. Thus, necroptosis is unlikely to mediate motor neuron degeneration in ALS patients.

Based on multiple, but disparate, lines of evidence implicating possible ferroptosis in ALS, including iron overload, GSH depletion and lipid peroxidation in affected CNS tissues, we interrogated key markers of ferroptotic pathway induction. GPX4 is the master regulator of ferroptosis and GPX4 depletion heralds activation of ferroptosis [20, 21, 38, 39]. GPX4 was abundantly expressed in spinal cords of control cases (Fig. 1b). Strikingly, GPX4 protein levels were reduced by ~55% ($p < 0.0001$) in fALS and ~80% in sALS ($p < 0.0001$), compared to control spinal cords, when normalised to β-actin (Fig. 1c). When normalised to βIII-tubulin as a neuronal loading control to account for neurodegeneration, GPX4 levels were diminished in spinal cords by 50% in fALS ($p < 0.01$) and ~70% in sALS ($p < 0.001$) (Fig. 1d). Thus, GPX4 is profoundly downregulated in spinal cords of both fALS and sALS, consistent with ferroptosis induction.

Anti-ferroptotic defence is compromised in affected CNS tissues of SOD1^{G93A} mice

To establish the expression of ferroptosis regulators throughout the disease course, we immunoblotted affected CNS tissues of SOD1^{G93A} mice at presymptomatic postnatal day 60 (P60), disease onset (P90), symptomatic (P120) and endstage (P150) ages (Fig. 2a). GPX4 protein levels were decreased by ~25% at P60 ($p < 0.05$), ~20% at P90, ~25% at P120 ($p < 0.001$) and ~45% at P150 ($p < 0.0001$) in spinal cords of SOD1^{G93A} mice, relative to age-matched WT littermate mice (Fig. 2b). Hence, GPX4 depletion in spinal cords of SOD1^{G93A} mice is early and progressive. In addition, GPX4 protein levels were also repressed by 30% at P60 ($p < 0.01$) and 25% at P90 ($p < 0.001$) in the forebrain of SOD1^{G93A} mice (Fig. 2b). Interestingly, GPX4 downregulation was not reflected at the transcriptional level for both total and mitochondrial (mGPX4) isoforms, suggesting a post-translational mechanism driving GPX4 depletion in spinal cord (Fig. 2c). Nuclear GPX4 (nGPX4) was not detected in spinal cord as expected.

Ferroptosis can also be orchestrated by iron metabolism dysregulation [40, 41] and therefore, both ferritin heavy chain 1 (FTH1) and TRF1 levels were measured to confirm ferroptosis. Critically, FTH1 expression was downregulated in the spinal cord by 25% ($p < 0.01$), whilst TFR1 expression level was reduced by ~25% ($p < 0.05$) in the forebrain of SOD1^{G93A} mice (Fig. 2d–g), coupling iron dysregulation to GPX4 depletion.

To investigate mechanisms underlying GPX4 depletion in SOD1^{G93A} mice, we analysed the NRF2 pathway that is linked to ferroptosis by induction of target genes involved in GSH synthesis. NRF2 levels were significantly reduced in spinal cords of SOD1^{G93A} mice (Fig. 2h, i). Importantly, expression of GCLC, a key target of NRF2 and enzyme critical for GSH synthesis was decreased in spinal cords of SOD1^{G93A} mice, consistent with diminished GSH levels in ALS [27]. Thus, an impaired NRF2 pathway and GSH synthesis is linked to GPX4 depletion in mutant SOD1 mice.

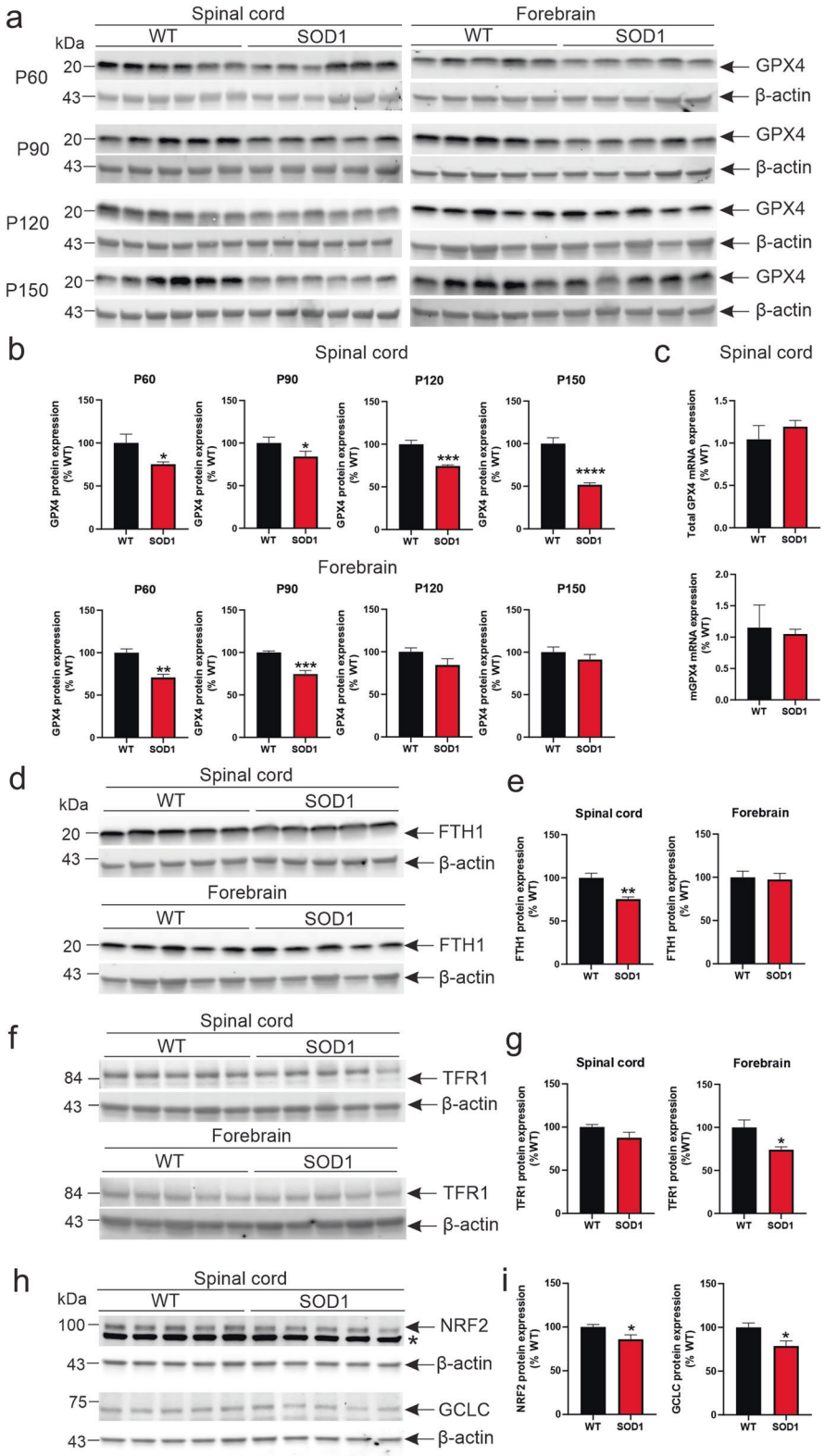

Fig. 2 GPX4 loss is common in spinal cords and brains of mouse models of ALS. a Immunoblot analysis and **b** quantification of GPX4 protein levels in the spinal cord and forebrain of WT and SOD1^{G93A} mice from postnatal day (P) 60–150. *$p < 0.05$, **$p < 0.01$, ***$p < 0.001$, ***$p < 0.0001$; Student's unpaired *t*-test. Data represent mean ± SEM, $n = 5$ mice per group. **c** mRNA expression of total GPX4 and mitochondrial (mGPX4) in WT and SOD1^{G93A} mice at P150. Data represent mean ± SEM, $n = 5$ mice per group. **d**–**g** Immunoblot analysis and quantification of FTH1 and TFR1 protein levels in the spinal cord of SOD1^{G93A} mice at P90. **$p < 0.01$, Student's unpaired *t*-test. Data represent mean ± SEM, $n = 5$ mice per group. **h**, **i** Immunoblot analysis and quantification of NRF2 and GCLC in the spinal cords of P120 WT and SOD1^{G93A} mice. *$p < 0.05$, Student's unpaired *t*-test. Data represent mean ± SEM, $n = 5$ mice per group. *non-specific band.

Anti-ferroptotic defence is impaired in affected CNS tissues of TDP-43^{Q331K} and C9orf72^{500} mice

To extend our findings, two additional ALS mouse models, transgenic TDP-43^{Q331K} and C9orf72^{500} mice, were examined for ferroptosis activation at disease onset (P240 and P300, respectively). Similarly, GPX4 was downregulated in spinal cord and forebrain of TDP-43^{Q331K} mice by ~20% ($p < 0.001$) and ~20% ($p < 0.05$), respectively (Fig. 3a, b). Moreover, GPX4 levels were also depleted in spinal cord and forebrain of C9orf72^{500} mice by ~20% ($p < 0.05$) and ~10% ($p < 0.05$), respectively (Fig. 3c, d). In line with iron dysregulation during ALS pathology, FTH1 levels were also reduced in the spinal cord and brain ($p < 0.05$) of TDP-43^{Q331K} mice (Fig. 3e, f). Moreover, TFR1 expression was decreased in spinal cord and brain ($p < 0.01$) of TDP-43^{Q331K} mice (Fig. 3g, h). TFR1 levels also fell by 25% in the spinal cord of C9orf72^{500} mice ($p < 0.05$), but not brain, in comparison to WT controls (Fig. 3i, j). Altogether, these findings suggest that GPX4 inactivation and iron dysregulation in vulnerable CNS regions is common in multiple mouse models of ALS.

Generation of transgenic human GPX4 mice

Given that GPX4 is the central repressor of ferroptosis, we sought to investigate the impact of inhibiting ferroptosis in ALS by elevating GPX4 levels in vivo. We first constructed and characterised novel transgenic mice expressing a human BAC containing human *GPX4* by a PiggyBac-on-BAC approach. First, a 185 kb BAC containing the entire human *GPX4* locus was identified, and through homologous recombination, a 3′-ITR-ampicillin selection cassette was introduced 20 kb downstream of human *GPX4* to remove adjacent *ARHGAP45* and *SBNO2* genes. The 5′-ITR-kanamycin selection cassette was next introduced 10 kb upstream of human *GPX4* using homologous recombination, removing the adjacent *POLRE2* gene. The modified BAC was then treated with BPase to excise the BAC transgene that expresses only human GPX4 that integrates into a single transposon site (Fig. 4a). This contrasts with a previously generated transgenic human GPX4 mouse line that used ~30 kb of 5′-flanking sequence and 20 kb of 3′-flanking sequence containing these genes [42]. Following pronuclear microinjection, four transgenic founder mice (lines 1–4) were identified from 56 pups. Transgenic GPX4 mice showed normal breeding, development, Mendelian inheritance of the transgene and were otherwise healthy and fertile.

We thereby performed PCR to confirm the human GPX4 BAC transgene detection in tail samples of founder mice. As indicated, human GPX4 was present in all four transgenic mouse lines, but not WT (Fig. 4b). Next, total GPX4 protein expression levels were screened in CNS tissues of each transgenic line with an anti-GPX4 antibody that recognises both murine and human forms. Given the high amino acid sequence identity of murine and human GPX4 (94%) and lack of specific reagents to detect only human GPX4, we determined expression owing to elevated GPX4 in transgenic lines. Out of three lines examined, line 1 showed the highest expression of GPX4 in spinal cord and forebrain, with a ~2-fold greater expression compared to WT mice ($p < 0.0001$) (Fig. 4c–f). Hence, line 1 mice were used as a model of human GPX4 overexpression. The tissue distribution of GPX4 was next determined in line 1 mice. In accordance with its ubiquitous expression and essential role in anti-oxidant defence, GPX4 protein was overexpressed in the heart, liver, kidney, spleen, gastrocnemius and tibialis anterior muscles, in addition to forebrain and spinal cord, compared to WT mice (Fig. 4g, h).

Cellular localisation of GPX4 protein was next examined in spinal cords of mice using immunohistochemistry. GPX4 was cytoplasmic and mainly localised to spinal motor neurons identified by their large diameter >20 µm, ventral horn location and NeuN-immunoreactivity in WT mice (Fig. 4i). GPX4 was also weakly expressed in NeuN-negative cells. In line 1 mice, GPX4 overexpression in motor neurons was confirmed, in addition to NeuN-negative cells consistent with the morphology of oligodendrocytes. Collectively, our data validate GPX4 overexpression in line 1 mice, especially in spinal motor neurons relevant to ALS.

GPX4 overexpression improves lifespan, motor function and delays disease onset in SOD1^{G93A} mice

To investigate the impact of inhibiting ferroptosis in ALS, we studied the effects of overexpressing human GPX4 on the phenotype of SOD1^{G93A} mice. As GPX4 function is critical for protection against ferroptosis, we hypothesised that if ferroptosis contributes to pathogenesis in SOD1^{G93A} mice, then its overexpression would significantly ameliorate disease signs in this model of ALS. SOD1^{G93A} mice were crossbred with transgenic GPX4 mice to generate four genotypes for analysis: SOD1^{G93A}; GPX4, SOD1^{G93A}, GPX4, and WT.

We studied female and male mice separately and assessed body weight and motor performance weekly using the rotarod test. Firstly, in terms of body weights, the growth of both female and male transgenic GPX4 mice was similar to WT animals (Fig. 5a, b), demonstrating that GPX4 overexpression was not harmful. Both female and male SOD1^{G93A} mice showed a progressive decline in weight loss, reflecting muscle wasting. Overexpression of GPX4 in male SOD1^{G93A} mice significantly delayed the age of peak body weight preceding weight decline (Fig. 5d) ($p < 0.05$) (126 ± 1.5 days, mean ± SEM), compared to SOD1^{G93A} males (118.3 ± 2.6 days). However, the same difference was not observed between female SOD1^{G93A};GPX4 (117.9 ± 1.4 days) and SOD1^{G93A} (117.8 ± 3.6 days) mice ($p = 0.96$) (Fig. 5c).

Locomotor function assessed by rotarod analysis was similar for both female and male WT and transgenic GPX4 mice, suggesting that GPX4 mice exhibit normal motor behaviour. In line with our previous findings [12], both sexes of SOD1^{G93A} mice showed a progressive decline in rotarod performance over time. Strikingly, overexpression of GPX4 preserved motor performance in both female ($p < 0.001$) (Fig. 5e) and male SOD1^{G93A} mice ($p < 0.05$) (Fig. 5f). Furthermore, post hoc analysis revealed that GPX4 elevation in female SOD1^{G93A} mice improved locomotor function at P88 ($p < 0.05$), P95 ($p < 0.01$) and P109 ($p < 0.05$), compared to SOD1^{G93A} mice.

Disease onset, which was determined retrospectively by the age of peak motor performance, was also improved by the overexpression of GPX4 in female SOD1^{G93A}; GPX4 (89.8 ± 4.2 days) when compared to SOD1^{G93A} mice (78.1 ± 3.1 days) mice ($p < 0.01$) (Fig. 5g). In addition, overexpression of GPX4 also delayed disease onset of male SOD1^{G93A}; GPX4 mice (78.1 ± 3.0 days), in comparison to SOD1^{G93A} mice (70.1 ± .8 days) ($p < 0.05$) (Fig. 5h). Thus, enhanced GPX4 expression improves motor function and delays disease onset of SOD1^{G93A} mice.

Critically, the overexpression of GPX4 extended survival of female SOD1^{G93A} mice by ~2 weeks, compared to SOD1^{G93A} mice ($p < 0.01$) (Fig. 5i). Consistently, survival of male SOD1^{G93A}; GPX4 mice (144.5 ± 3.6 days) was higher than SOD1^{G93A} mice (136.3 ± 2.6 days) ($p = 0.08$) (Fig. 5j). Combined, our findings suggest that overexpression of GPX4 increased lifespan of SOD1^{G93A} mice by delaying disease onset.

GPX4 overexpression is neuroprotective and anti-ferroptotic in SOD1^{G93A} mice

GPX4 overexpression was next confirmed in spinal cords of our mouse cohorts. Transgenic GPX4 mice showed elevated GPX4 expression as expected ($p < 0.0001$) (Fig. 6a, b). Consistently, GPX4 levels were reduced by ~40% in SOD1^{G93A} mice, compared to WT ($p < 0.001$). Importantly, SOD1^{G93A}; GPX4 mice showed ~25% higher GPX4 expression, compared to SOD1^{G93A} controls ($p < 0.05$), validating GPX4 overexpression in ALS mice. Human SOD1 levels were similar in SOD1^{G93A} and SOD1^{G93A}; GPX4 mice. GPX4 overexpression was then confirmed at the level of motor neurons in spinal cord. In line with our western blot findings, GPX4 levels

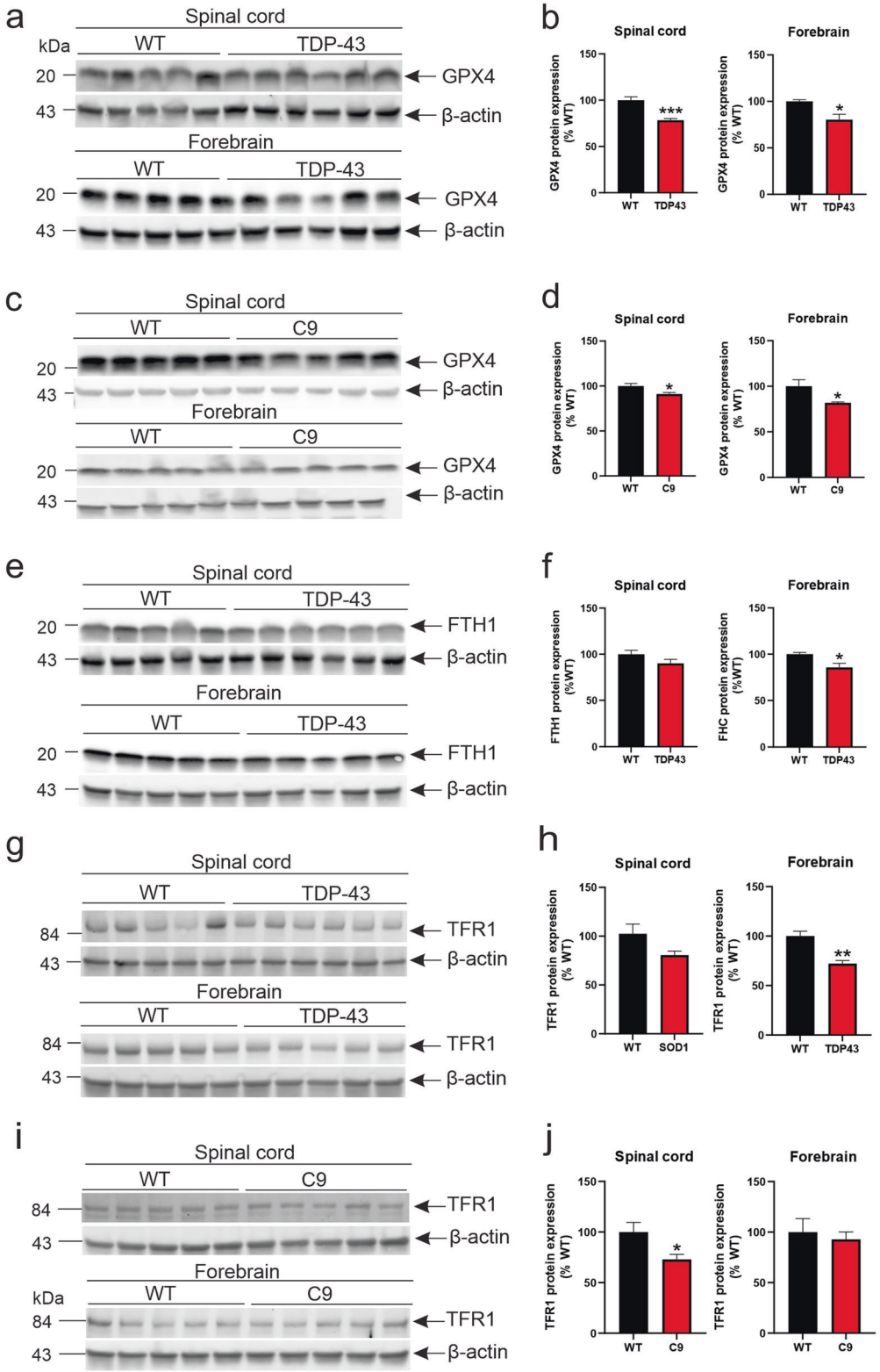

Fig. 3 Anti-ferroptosis defence is impaired in affected CNS tissues of TDP-43^{Q331K} and C9orf72^{500} mice. Immunoblot analysis and quantification of GPX4 protein levels in the spinal cord and forebrain of WT and **a**, **b** TDP-43^{Q331K} at P240, and **c**, **d** C9orf72^{500} mice at P300. Immunoblot analysis and quantification of FTH1 and TFR1 protein levels in the spinal cord of **e**–**h** TDP-43^{Q331K} and **i**, **j** C9orf72500 mice. *$p <$ 0.05, **$p < 0.01$, ***$p < 0.001$; Student's unpaired *t*-test. Data represent mean ± SEM, $n = 5$–6 mice per group.

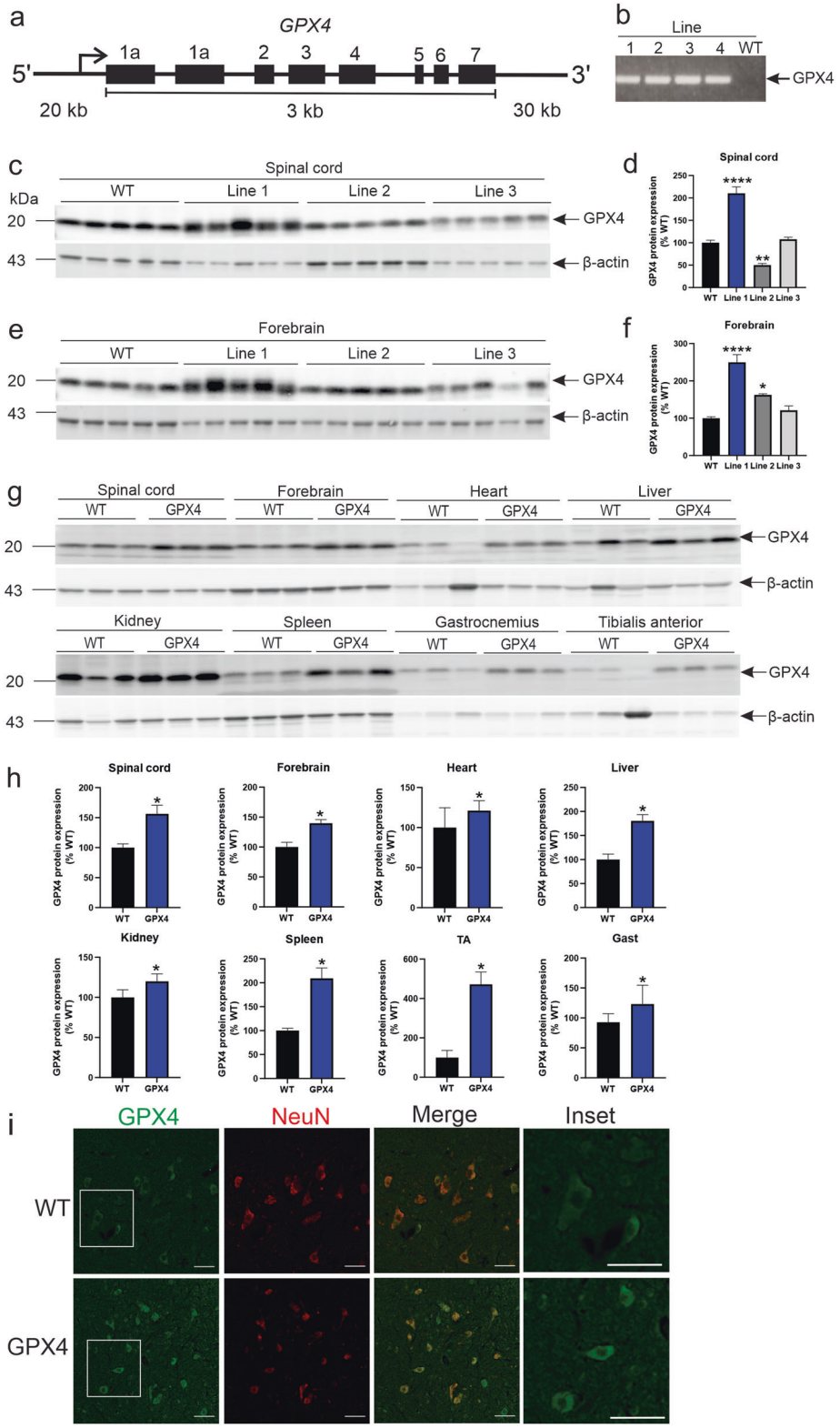

Fig. 4 Characterisation of transgenic human GPX4 mice. a Human *GPX4* BAC transgene map including 20 kb upstream and 30 kb downstream genomic sequence. **b** Gel PCR of GPX4 transgene detection in mice. Immunoblot and quantification of GPX4 protein levels normalised to β-actin, relative to WT mice in **c**, **d** spinal cord and **e**, **f** forebrain of GPX4 mice at P30. $*p < 0.05$, $**p < 0.01$, $****p < 0.0001$; Student's unpaired *t*-test. Data represent mean ± SEM, $n = 5$ mice per group. **g**, **h** Immunoblot and quantification of GPX4 protein expression relative to WT mice in various tissues of GPX4 mice at P180–200. $*p < 0.05$; Student's unpaired *t*-test. Data represent mean ± SEM, $n = 3$ mice per group. **i** Representative GPX4 immunohistochemical analysis of ventral horn sections of spinal cords of WT and GPX4 mice. Scale bars, 50 µm.

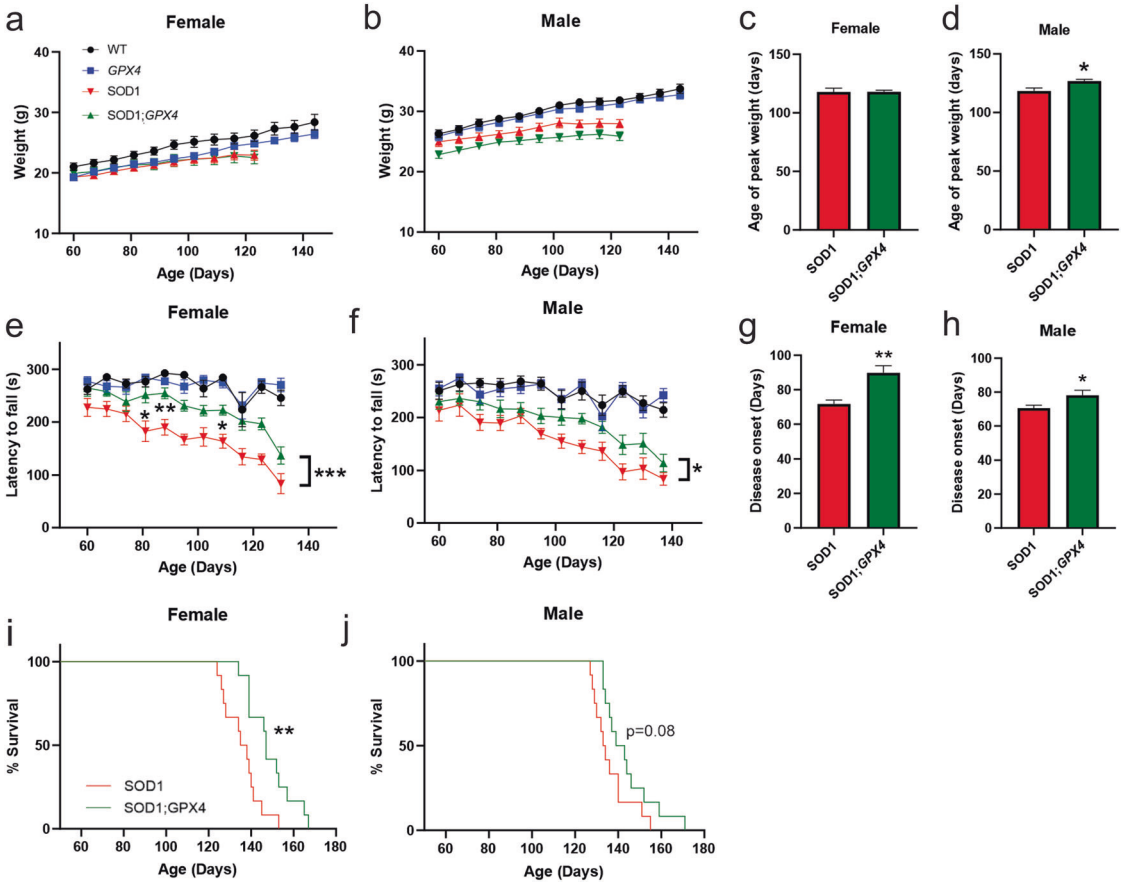

Fig. 5 GPX4 overexpression delays weight loss, improves locomotor function and survival in SOD1^{G93A} mice. Body weights of **a** female and **b** male WT, GPX4, SOD1^{G93A} and SOD1^{G93A}; GPX4 mice. Age of peak body weight of **c** female and **d** male SOD1^{G93A} and SOD1^{G93A}; GPX4 mice. Data represent mean ± SEM, $n = 12$ mice per group, $^{*}p < 0.05$, Student's *t*-test. Locomotor function of **e** female and **f** male WT, GPX4, SOD1^{G93A} and SOD1^{G93A}; GPX4 mice determined by latency to fall using weekly rotarod analysis. $^{*}p < 0.05$, $^{**}p < 0.01$, $^{***}p < 0.001$, two-way ANOVA, Sidak's post hoc analysis. Age of peak rotarod performance of **g** female and **h** male SOD1^{G93A} and SOD1^{G93A}; GPX4 mice. Data represent mean ± SEM, $n = 12$ mice per group, $^{*}p < 0.05$, $^{**}p < 0.01$, Student's *t*-test. Kaplan–Meier survival analysis of **i** female and **j** male mice determined by onset of hindlimb paralysis in SOD1^{G93A} and SOD1^{G93A}; GPX4 mice, $n = 12$ mice per group, $^{**}p < 0.01$.

were higher in motor neurons of transgenic GPX4 mice, compared to WT (Fig. 6c). In addition, GPX4 levels were augmented in motor neurons of SOD1^{G93A}; GPX4 mice, relative to SOD1^{G93A} mice.

To determine the anti-ferroptotic action of GPX4 overexpression in this mouse model, we quantified motor neuron death in the spinal cord using cresyl violet staining (Fig. 6d). Motor neuron numbers were similar in WT and GPX4 mice, demonstrating that GPX4 mice are neuropathologically normal. Motor neuron counts were reduced by 40% in SOD1^{G93A} mice, compared to WT animals. Notably, GPX4 overexpression significantly prevented motor neuron loss in SOD1^{G93A} mice (Fig. 6e). MDA levels were next measured in the CNS of mice as a marker of lipid peroxidation. SOD1^{G93A} mice showed accumulation of MDA levels, while transgenic GPX4 animals revealed lower levels of MDA (Fig. 6f). Importantly, lipid peroxidation was significantly attenuated in the CNS of SOD1^{G93A}; GPX4 mice ($p < 0.05$), confirming anti-oxidant and anti-ferroptotic actions of GPX4 overexpression. Thus, GPX elevation improves motor function and lifespan of SOD1^{G93A} mice by inhibiting ferroptosis and motor neuron death.

DISCUSSION

Selective motor neuron loss in ALS has been attributed to multiple cell death pathways, including apoptosis, ER stress-induced cell death, autophagic cell death and necroptosis. Pharmacological inhibition and genetic ablation studies in humanised cell co-culture models of ALS have identified non-apoptotic modes of motor neuron death [5]. Here, we establish that ferroptosis, a recently described iron-dependent RCD pathway [43], mediates selective motor neuron death in ALS. Multiple lines of evidence accumulated over decades, including iron accumulation [22–24], anti-oxidant imbalance [25, 27] and lipid peroxidation [29, 30] in affected CNS regions of ALS implicate ferroptosis. Furthermore, human-induced pluripotent stem cell-derived motor neurons were recently identified to undergo ferroptosis in vitro [44], while neuronal *Gpx4* ablation triggered motor neuron death and paralysis in mice [31]. Lastly, blood markers of ferroptosis, including lipid peroxides, ferritin and transferrin, correlated with ALS prognosis [45]. We believe that depletion of GPX4, the critical anti-ferroptotic enzyme, discovered here is the convergence point for iron overload, glutathione imbalance and lipid peroxidation in ALS, uniting these disparate observations.

We recently determined that necroptosis was dispensable for motor neuron death in SOD1^{G93A} mice, in accordance with two other studies [10, 11]. RIPK3 and MLKL were not detectable at transcript or protein levels in the CNS of SOD1^{G93A} mice in our study [12], as corroborated by another group [11]. Here, we were unable to detect RIPK1 and MLKL in spinal cords of ALS patients and healthy controls. This result contrasts with an original report of RIPK1, RIPK3 and MLKL accumulation and activation in spinal cords in ALS [9]. Although this could reflect differences in ALS patient cohorts, such as disease heterogeneity, tissue collection

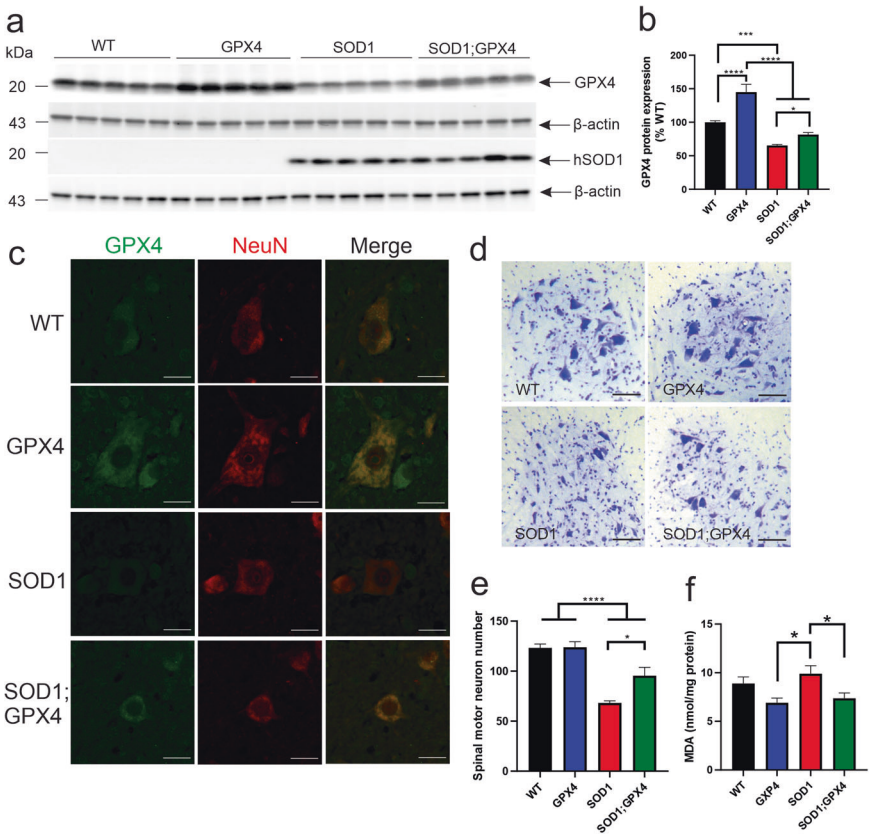

Fig. 6 Protection from ferroptosis rescues motor neuron loss in SOD1^{G93A} mice. a Immunoblot analysis and **b** quantification of GPX4 protein levels in the spinal cord of WT, GPX4, SOD1^{G93A} and SOD1^{G93A};GPX4 mice at clinical endstage. **c** Representative GPX4 immunohistochemical analysis of spinal motor neurons in mice. Scale bars, 20 µm. **d** Representative photomicrographs and **e** quantification of lumbar spinal cords of mice stained with cresyl violet at clinical endstage. *$p < 0.05$, ***$p < 0.001$, ****$p < 0.0001$; one-way ANOVA with Dunnett's post hoc test. Data represent mean ± SEM, $n = 5$ per genotype. Scale bars, 50 µm. **f** Quantification of malondialdehyde (MDA) accumulation in forebrains of mice at clinical endstage. *$p < 0.05$, one-way ANOVA with Bonferroni post hoc test. Data represent mean ± SEM, $n = 5$ per genotype.

and preparation, it is possible that blood-borne cells and immune cell infiltration could contribute to necroptotic marker signal in the CNS, rather than reflecting genuine neuronal or glial cell necroptosis. This is especially likely considering that necroptosis effectors are expressed abundantly in the haematopoietic compartment [46–48]. Our inability to detect MLKL transcripts in motor neurons of mouse tissue supports this contention [12].

GPX4 depletion was common to both familial and sporadic ALS patients and three distinct genetic mouse models of ALS, arguing that GPX4 dysregulation is universal in ALS. GPX4 downregulation was not a consequence of neurodegeneration as GPX4 levels fell early in spinal cords and cortices of SOD1^{G93A} mice, preceding symptoms and motor neuron loss. GPX4 was mainly localised to motor neurons in spinal cords, consistent with a previous study [31], suggesting a cell-autonomous effect of GPX4 depletion and ferroptosis within motor neurons. Expression of the glutamate/cystine antiporter xCT is necessary for ferroptosis. While xCT expression is mainly associated with microglia which suggests microglial ferroptosis [28], it was recently reported that xCT is also expressed by human-induced pluripotent stem cell-derived motor neurons [44] and spinal motor neurons of mice [49]. Collectively, these findings implicate motor neuron ferroptosis in ALS.

The mechanism(s) responsible for GPX4 depletion in ALS remain unresolved, although we ruled out transcriptional repression in spinal cords of SOD1^{G93A} mice, implicating post-translational regulation. As GPX4 translation and activity are regulated by its co-factors GSH and selenium [14], it is possible that GSH biosynthesis, uptake or selenium availability is impaired in motor neurons in ALS. GSH depletion and cystine/glutamate antiporter system x_c^- dysregulation occurs in spinal cords of mutant SOD1 mice [27, 28], supporting this idea. Indeed, we determined impaired NRF2 pathway signalling and GCLC levels associated with GPX4 depletion in SOD1^{G93A} mice, favouring diminished GSH synthesis. Alternatively, GPX4 is a substrate for chaperone-mediated autophagy [50] and accelerated clearance by this catabolic pathway may account for GPX4 depletion in ALS. GPX4 depletion is also a feature of vulnerable neurons in Parkinson's disease [51] and stroke [52], suggesting an important sensitising role of ferroptosis and cell death in both acute and chronic neurodegenerative disorders.

To confirm a direct role of ferroptosis in mediating motor neuron death in vivo, we constructed novel BAC transgenic human GPX4 mice. These mice overexpressed human GPX4 in all tissues assessed, principally in spinal cord, brain and skeletal muscle, consistent with the essential anti-oxidant and anti-ferroptotic role of GPX4 in the neuromuscular system [31]. SOD1^{G93A} mice were crossbred with transgenic GPX4 mice, revealing ameliorated symptoms and pathology in double transgenic mice. Importantly, GPX4 overexpression extended survival by delaying disease onset, again consistent with cell-autonomous effects in ALS [53]. In support of this, GPX4 overexpression countered motor neuron death in SOD1^{G93A};GPX4 mice, demonstrating a direct role of ferroptosis in executing cell death in ALS. Our findings accord with a recent study that crossed SOD1^{G93A} mice with an independent transgenic GPX4 line that also delayed disease onset and rescued motor neurons [32].

Interestingly, GPX1 deficiency or overexpression in SOD1^{G93A} mice did not modify disease [54], illustrating the exquisite specificity of GPX4 for inhibiting ferroptosis in ALS.

Our findings demonstrating that GPX4 overexpression is neuroprotective in SOD1^{G93A} mice have clear therapeutic implications for ALS. Strategies that induce or upregulate GPX4 expression may be useful to explore in ALS, including selenium treatment. Intracerebroventricular injection of selenium induced brain GPX4 levels, countered ferroptosis and improved functional outcomes in a mouse model of stroke [55]. Furthermore, systemic injection of brain-penetrant selenopeptides induced GPX4 expression and blocked ferroptotic cell death in mice with stroke [55]. Hence, increasing selenium availability may be a useful pharmacological approach to augment the anti-ferroptotic activity of GPX4 in ALS to counter neurodegeneration. Our findings are also consistent with the proposed mechanism of action of CuATSM, currently completing a phase 3 clinical trial for ALS. CuATSM robustly and reproducibly rescues ALS mouse models [56, 57]. CuATSM is also potent inhibitor of ferroptosis [58], consistent with targeting the pathogenic mechanism we describe here. Lastly, iron chelation therapy with deferoxamine in SOD1^{G93A} mice [59] and deferiprone in SOD1^{G86R} mice and ALS patients [60] was reported to be beneficial and is expected to mitigate iron overload triggered ferroptosis, although ferroptosis was not examined in either study.

In summary, this study demonstrates that anti-ferroptotic defence mediated by GPX4 is impaired in vulnerable CNS tissues of ALS patients and multiple mouse models. GPX4 overexpression restored ferroptosis defence, inhibiting lipid peroxidation and motor neuron death and improving motor function and outcome. Pharmacological targeting and activation of the GPX4 pathway therefore represents a promising approach for potential effective treatment of ALS.

DATA AVAILABILITY

Original data are available upon request to BJT (bradley.turner@florey.edu.au).

REFERENCES

1. Brown RH, Al-Chalabi A. Amyotrophic lateral sclerosis. N Engl J Med. 2017;337:162–72.
2. Taylor JP, Brown RH, Cleveland DW. Decoding ALS: from genes to mechanism. Nature. 2016;539:197–206.
3. Galluzzi L, Vitale I, Aaronson SA, Abrams JM, Adam D, Agostinis P, et al. Molecular mechanisms of cell death: recommendations of the Nomenclature Committee on Cell Death 2018. Cell Death Differ. 2018;25:486–541.
4. Aebischer J, Bernard-Marissal N, Pettmann B, Raoul C. Death receptors in the selective degeneration of motoneurons in amyotrophic lateral sclerosis. J Neurodegener Dis. 2013;2013:746845. https://doi.org/10.1155/2013/746845.
5. Re DB, Le Verche V, Yu C, Amoroso MW, Politi KA, Phani S, et al. Necroptosis drives motor neuron death in models of both sporadic and familial ALS. Neuron. 2014;81:1001–8.
6. Dzhashiashvili Y, Monckton CP, Shah HS, Kunjamma RB, Popko B. The UPR-PERK pathway is not a promising therapeutic target for mutant SOD1-induced ALS. Neurobiol Dis. 2019;127:527–44.
7. Samson AL, Garnish SE, Hildebrand JM, Murphy JM. Location, location, location: a compartmentalized view of TNF-induced necroptotic signaling. Sci Signal. 2021;14:eabc6178. https://doi.org/10.1126/scisignal.abc6178.
8. Chevin M, Sébire G. Necroptosis in ALS: a hot topic in-progress. Cell Death Discov. 2021;7:1.
9. Ito Y, Ofengeim D, Najafov A, Das S, Saberi S, Li Y, et al. RIPK1 mediates axonal degeneration by promoting inflammation and necroptosis in ALS. Science. 2016;353:603–8.
10. Dominguez S, Varfolomeev E, Brendza R, Stark K, Tea J, Imperio J, et al. Genetic inactivation of RIP1 kinase does not ameliorate disease in a mouse model of ALS. Cell Death Differ. 2021;28:915–31.
11. Dermentzaki G, Politi KA, Lu L, Mishra V, Pérez-Torres EJ, Sosunov AA, et al. Deletion of Ripk3 prevents motor neuron death in Vitro but not in Vivo. eNeuro. 2019;6:1–16.
12. Wang T, Perera ND, Chiam MDF, Cuic B, Wanniarachchillage N, Tomas D, et al. Necroptosis is dispensable for motor neuron degeneration in a mouse model of ALS. Cell Death Differ. 2020;27:1728–39.
13. Dixon SJ, Stockwell BR. The role of iron and reactive oxygen species in cell death. Nat Chem Biol. 2014;10:9–17.
14. Chen X, Li J, Kang R, Klionsky DJ, Tang D. Ferroptosis: machinery and regulation. Autophagy. 2021;17:2054–81.
15. Tang D, Chen X, Kang R, Kroemer G. Ferroptosis: molecular mechanisms and health implications. Cell Res. 2021;31:107–25.
16. Hou W, Xie Y, Song X, Sun X, Lotze MT, Zeh HJ, et al. Autophagy promotes ferroptosis by degradation of ferritin. Autophagy. 2016;12:1425–8.
17. Park E, Chung SW. ROS-mediated autophagy increases intracellular iron levels and ferroptosis by ferritin and transferrin receptor regulation. Cell Death Dis. 2019;10:822.
18. Wirth EK, Conrad M, Winterer J, Wozny C, Carlson BA, Roth S, et al. Neuronal selenoprotein expression is required for interneuron development and prevents seizures and neurodegeneration. FASEB J. 2010;24:844–52.
19. Seiler A, Schneider M, Förster H, Roth S, Wirth EK, Culmsee C, et al. Glutathione peroxidase 4 senses and translates oxidative stress into 12/15-lipoxygenase dependent- and AIF-mediated cell death. Cell Metab. 2008;8:237–48.
20. Yang WS, Sriramaratnam R, Welsch ME, Shimada K, Skouta R, Viswanathan VS, et al. Regulation of ferroptotic cancer cell death by GPX4. Cell. 2014;156:317–31. https://doi.org/10.1016/j.cell.2013.12.010.
21. Friedmann Angeli JP, Schneider M, Proneth B, Tyurina YY, Tyurin VA, Hammond VJ, et al. Inactivation of the ferroptosis regulator Gpx4 triggers acute renal failure in mice. Nat Cell Biol. 2014;16:1180–91. https://doi.org/10.1038/ncb3064.
22. Oba H, Araki T, Ohtomo K, Monzawa S, Uchiyama G, Koizumi K, et al. Amyotrophic lateral sclerosis: T2 shortening in motor cortex at MR imaging. Radiology. 1993;189:843–6.
23. Kasarskis EJ, Tandon L, Lovell MA, Ehmann WD. Aluminum, calcium, and iron in the spinal cord of patients with sporadic amyotrophic lateral sclerosis using laser microprobe mass spectroscopy: a preliminary study. J Neurol Sci. 1995;130:203–8.
24. Suh YJ, Rathore KI, Schulz K, Ponka P, Arosio P, David S. Dysregulation of iron homeostasis in the CNS contributes to disease progression in a mouse model of amyotrophic lateral sclerosis. J Neurosci. 2009;29:610–19.
25. Choi IY, Lee P, Statland J, McVey A, Dimachkie M, Brooks W, et al. Reduction in cerebral antioxidant, glutathione (GSH), in patients with ALS: a preliminary study. Neurology. 2015;84:P6.105.
26. Khan M, Sekhon B, Jatana M, Giri S, Gilg AG, Sekhon C, et al. Administration of N-acetylcysteine after focal cerebral ischemia protects brain and reduces inflammation in a rat model of experimental stroke. J Neurosci Res. 2004;76:519–27.
27. Chi L, Ke Y, Luo C, Gozal D, Liu R. Depletion of reduced glutathione enhances motor neuron degeneration in vitro and in vivo. Neuroscience. 2007;144:991–1003.
28. Mesci P, Zaïdi S, Lobsiger CS, Millecamps S, Escartin C, Seilhean D, et al. System xC- is a mediator of microglial function and its deletion slows symptoms in amyotrophic lateral sclerosis mice. Brain. 2015;138:53–68.
29. Ferrante RJ, Shinobu LA, Schulz JB, Matthews RT, Thomas CE, Kowall NW, et al. Increased 3-Nitrotyrosine and oxidative damage in mice with a human copper/zinc superoxide dismutase mutation. Ann Neurol. 1997;42:326–34.
30. Pedersen WA, Fu W, Keller JN, Markesbery WR, Appel S, Smith RG, et al. Protein modification by the lipid peroxidation product 4-hydroxynonenal in the spinal cords of amyotrophic lateral sclerosis patients. Ann Neurol. 1998;44:819–24.
31. Chen, Hambright WS, Na R, Ran Q. Ablation of the ferroptosis inhibitor glutathione peroxidase 4 in neurons results in rapid motor neuron degeneration and paralysis. J Biol Chem. 2015;290:28097–106.
32. Chen L, Na R, Danae McLane K, Thompson CS, Gao J, Wang X, et al. Overexpression of ferroptosis defense enzyme Gpx4 retards motor neuron disease of SOD1G93A mice. Sci Rep. 2021;11:1–13.
33. Scott S, Kranz JE, Cole J, Lincecum JM, Thompson K, Kelly N, et al. Design, power, and interpretation of studies in the standard murine model of ALS. Amyotroph Lateral Scler. 2008;9:4–15.
34. Petrie EJ, Sandow JJ, Jacobsen AV, Smith BJ, Griffin MDW, Lucet IS, et al. Conformational switching of the pseudokinase domain promotes human MLKL tetramerization and cell death by necroptosis. Nat Commun. 2018;9:2422.
35. Hu CL, Nydes M, Shanley KL, Morales Pantoja IE, Howard TA, Bizzozero OA. Reduced expression of the ferroptosis inhibitor glutathione peroxidase-4 in multiple sclerosis and experimental autoimmune encephalomyelitis. J Neurochem. 2019;148:426–39.
36. Rao X, Huang X, Zhou Z, Lin X. An improvement of the 2ˆ(-delta delta CT) method for quantitative real-time polymerase chain reaction data analysis. Biostat Bioinforma Biomath. 2013;3:71–85.

37. Samson AL, Zhang Y, Geoghegan ND, Gavin XJ, Davies KA, Mlodzianoski MJ, et al. MLKL trafficking and accumulation at the plasma membrane control the kinetics and threshold for necroptosis. Nat Commun. 2020;11:3151.
38. Dixon SJ, Stockwell BR. The hallmarks of ferroptosis. Annu Rev Cancer Biol. 2019;3:35–54.
39. Forcina GC, Dixon SJ. GPX4 at the crossroads of lipid homeostasis and ferroptosis. Proteomics. 2019;19:1–11.
40. Lei P, Bai T, Sun Y. Mechanisms of ferroptosis and relations with regulated cell death: a review. Front Physiol. 2019;10:1–13.
41. Ding H, Chen S, Pan X, Dai X, Pan G, Li Z, et al. Transferrin receptor 1 ablation in satellite cells impedes skeletal muscle regeneration through activation of ferroptosis. J Cachexia Sarcopenia Muscle. 2021;12:746–68.
42. Ran Q, Liang H, Gu M, Qi W, Walter CA, Roberts LJ, et al. Transgenic mice overexpressing glutathione peroxidase 4 are protected against oxidative stress-induced apoptosis. J Biol Chem. 2004;279:55137–46.
43. Dixon SJ, Lemberg KM, Lamprecht MR, Skouta R, Zaitsev EM, Gleason CE, et al. Ferroptosis: an iron-dependent form of nonapoptotic cell death. Cell. 2012;149:1060–72.
44. Matsuo T, Adachi-Tominari K, Sano O, Kamei T, Nogami M, Ogi K, et al. Involvement of ferroptosis in human motor neuron cell death. Biochem Biophys Res Commun. 2021;566:24–29.
45. Devos D, Moreau C, Kyheng M, Garçon G, Rolland AS, Blasco H, et al. Author correction: A ferroptosis-based panel of prognostic biomarkers for Amyotrophic Lateral Sclerosis (Scientific Reports, (2019), 9, 1, (2918). Sci Rep. 2020;10:58956. https://doi.org/10.1038/s41598-019-39739-5.
46. Rickard JA, O'Donnell JA, Evans JM, Lalaoui N, Poh AR, Rogers T, et al. RIPK1 regulates RIPK3-MLKL-driven systemic inflammation and emergency hematopoiesis. Cell. 2014;157:1175–88.
47. Murphy JM, Czabotar PE, Hildebrand JM, Lucet IS, Zhang JG, Alvarez-Diaz S, et al. The pseudokinase MLKL mediates necroptosis via a molecular switch mechanism. Immunity. 2013;39:443–53.
48. Newton K, Sun X, Dixit VM. Kinase RIP3 is dispensable for normal NF-κBs, signaling by the B-cell and T-cell receptors, tumor necrosis factor receptor 1, and toll-like receptors 2 and 4. Mol Cell Biol. 2004;24:1464–9.
49. Sprimont L, Janssen P, De Swert K, Van Bulck M, Rooman I, Gilloteaux J, et al. Cystine–glutamate antiporter deletion accelerates motor recovery and improves histological outcomes following spinal cord injury in mice. Sci Rep. 2021;11:1–15.
50. Wu Z, Geng Y, Lu X, Shi Y, Wu G, Zhang M, et al. Chaperone-mediated autophagy is involved in the execution of ferroptosis. Proc Natl Acad Sci USA. 2019;116:2996–3005.
51. Bellinger FP, Bellinger MT, Seale LA, Takemoto AS, Raman AV, Miki T, et al. Glutathione peroxidase 4 is associated with neuromelanin in substantia nigra and dystrophic axons in putamen of Parkinson's brain. Mol Neurodegener. 2011;6:8. https://doi.org/10.1186/1750-1326-6-8.
52. Zhang, Wu Y, Yuan S, Zhang P, Zhang J, Li H, et al. Glutathione peroxidase 4 participates in secondary brain injury through mediating ferroptosis in a rat model of intracerebral hemorrhage. Brain Res. 2018;1701:112–25.
53. Boillée S, Yamanaka K, Lobsiger CS, Copeland NG, Jenkins NA, Kassiotis G, et al. Onset and progression in inherited ALS determined by motor neurons and microglia. Science. 2006;312:1389–92.
54. Cudkowicz ME, Pastusza KA, Sapp PC, Mathews RK, Leahy J, Pasinelli P, et al. Survival in transgenic ALS mice does not vary with CNS glutathione peroxidase activity. Neurology. 2002;59:729–34.
55. Alim I, Caulfield JT, Chen Y, Swarup V, Geschwind DH, Ivanova E, et al. Selenium drives a transcriptional adaptive program to block ferroptosis and treat stroke. Cell. 2019;177:1262–79.e25.
56. Soon CPW, Donnelly PS, Turner BJ, Hung LW, Crouch PJ, Sherratt NA, et al. Diacetylbis(N(4)-methylthiosemicarbazonato) copper(II) (Cu II(atsm)) protects against peroxynitrite-induced nitrosative damage and prolongs survival in amyotrophic lateral sclerosis mouse model. J Biol Chem. 2011;286:44035–44.
57. Roberts BR, Lim NKH, McAllum EJ, Donnelly PS, Hare DJ, Doble PA, et al. Oral treatment with Cull(atsm) increases mutant SOD1 in vivo but protects motor neurons and improves the phenotype of a transgenic mouse model of amyotrophic lateral sclerosis. J Neurosci. 2014;34:8021–31.
58. Southon A, Szostak K, Acevedo KM, Dent KA, Volitakis I, Belaidi AA, et al. Cull (atsm) inhibits ferroptosis: Implications for treatment of neurodegenerative disease. Br J Pharm. 2020;177:656–67.
59. Lee JK, Shin JH, Gwag BJ, Choi EJ. Iron accumulation promotes TACE-mediated TNF-α secretion and neurodegeneration in a mouse model of ALS. Neurobiol Dis. 2015;80:63–69.
60. Moreau C, Danel V, Devedjian JC, Grolez G, Timmerman K, Laloux C, et al. Could conservative iron chelation lead to neuroprotection in amyotrophic lateral sclerosis? Antioxid Redox Signal. 2018;29:742–8.

AUTHOR CONTRIBUTIONS

TW and BJT conceived the study. TW, DT, NDP, BC, SL, AV, SKB, ALS and AS conducted the experiments. TW, AS and BJT analysed the data. AIB, JMM and BJT supervised the study and interpreted data. CAM collected human post-mortem tissues. TW and BJT wrote the manuscript. All authors reviewed and edited the manuscript.

FUNDING

Funding for this project was provided by the Angie Cunningham FightMND PhD Scholarship and Grant (TW, BJT), Australian NHMRC (Fellowship 1137024 to BJT; Grant 2002965 to ALS; Fellowship 1172929 and IRIISS 9000653 to JMM), Rebecca L. Cooper Al & Val Rosenstrauss Medical Research Fellowship (SKB) and Stafford Fox Medical Research Foundation (BJT). Human spinal cord tissues were received from the Victorian Brain Bank, supported by The Florey, The Alfred, Victorian Institute of Forensic Medicine and Coroners Court of Victoria and funded in part by Parkinson's Victoria, MND Victoria, FightMND, Yulgilbar Foundation and Ian and Maria Cootes. The Florey Institute of Neuroscience & Mental Health and Walter & Eliza Hall Institute acknowledge Victorian Government Operational Infrastructure Support.

COMPETING INTERESTS

ALS and JMM contribute to a programme developing inhibitors of necroptosis with Anaxis Pharma Pty Ltd.

ETHICS APPROVAL

Work with human tissues was approved by the Medicine and Dentistry Human Ethics Sub-Committee (Project 18.36, ethics number 1852824). Animal studies were approved by the Florey Institute Animal Ethics Committee (permit numbers: 17-093 and 19-067).

ADDITIONAL INFORMATION

Supplementary information The online version contains supplementary material available at https://doi.org/10.1038/s41418-021-00910-z.

Correspondence and requests for materials should be addressed to Bradley J. Turner.

Reprints and permission information is available at http://www.nature.com/reprints

Publisher's note Springer Nature remains neutral with regard to jurisdictional claims in published maps and institutional affiliations.